

Article

Design of Tool Wear Monitoring System in Bone Material Drilling Process

 Lijia Liu ^{1,2,*}, Wenjie Kang ¹, Yiwen Wang ² and Lingchen Zeng ¹
¹ School of Automation, Harbin University of Science and Technology, Harbin 150080, China; kang1997123@gmail.com (W.K.); zlc505731668@163.com (L.Z.)

² Key Laboratory of Advanced Manufacturing and Intelligent Technology, Ministry of Education, Harbin University of Science and Technology, Harbin 150080, China; wyw@hrbust.edu.cn

* Correspondence: liulijia@hrbust.edu.cn

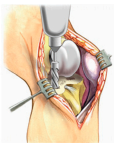
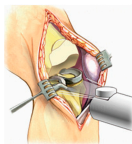
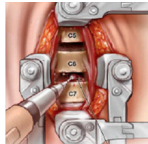





Abstract: Biological bone materials, complex and anisotropic, require precise machining in surgeries. Bone drilling, a key technique, is susceptible to increased friction from tool wear, leading to excessive forces and high temperatures that can damage bone and surrounding tissues, affecting recovery. This study develops a monitoring platform to assess tool wear during bone drilling, employing an experimental setup that gathers triaxial force and vibration data. A recognition model using a bidirectional long short-term memory network (BI-LSTM) with a multi-head attention mechanism identified wear levels. This model, termed ABI-LSTM, was optimized and benchmarked against SVR, RNN, and CNN models. The results from implementing the ABI-LSTM-based monitoring system demonstrated its efficacy in detecting tool wear, thereby potentially reducing surgical risks such as osteonecrosis and drill breakage, and enhancing surgical outcomes.

Keywords: bone drilling; tool wear; monitoring system; wavelet packet analysis; BI-LSTM

1. Introduction

Clinical orthopedic bone drilling, among the oldest surgical procedures in medical history, primarily involves drilling into bone tissue to place screws and other fixation devices. This technique has been refined by incorporating advances in mechanical engineering and processing theories into orthopedic surgeries, broadly categorizing them into mechanical and specialized energy field processing for bone material removal. Depending on the specific surgical requirements, these processes can further be subdivided into drilling, milling, grinding, and sawing—techniques commonly used in metal processing, as shown in Table 1 [1].

Table 1. Removal methods of machined bone materials.

Removal Methods	Drilling	Sawing	Milling	Grinding
Application Scenarios				
Cutters				

Presently, methods for removing bone tissue in surgeries have garnered significant research interest, especially due to the anisotropic nature of bone materials, which differ



Citation: Liu, L.; Kang, W.; Wang, Y.; Zeng, L. Design of Tool Wear Monitoring System in Bone Material Drilling Process. *Coatings* **2024**, *14*, 812. <https://doi.org/10.3390/coatings14070812>

Academic Editor: Ben Beake

Received: 28 April 2024

Revised: 7 June 2024

Accepted: 11 June 2024

Published: 28 June 2024



Copyright: © 2024 by the authors. Licensee MDPI, Basel, Switzerland. This article is an open access article distributed under the terms and conditions of the Creative Commons Attribution (CC BY) license (<https://creativecommons.org/licenses/by/4.0/>).

fundamentally from metals. The drilling environment is semi-enclosed, without the use of effective coolants typical in metal drilling, leading to potential thermal damage to bone tissue. It is widely accepted that the safe temperature threshold for human bones is below 47 °C; temperatures exceeding this during drilling can result in thermal injury, reduced biological activity, and ultimately, osteonecrosis or osteomyelitis [2]. Additionally, poor drilling quality can cause surface burrs and cracks, adversely affecting post-surgical recovery. Additionally, when the drill bit transitions from cortical to cancellous bone, a sudden change in drilling force can occur. If not well-managed by the surgeon, this can significantly disrupt the drilling process, potentially leading to drill bit breakage.

In clinical settings, drill bits are not disposable but reusable due to cost and biocompatibility considerations, typically made from wear-prone medical-grade stainless steel. After multiple uses, these tools inevitably wear down and require high-temperature and chemical sterilization post-surgery, leading to unavoidable chemical corrosion. Allan and colleagues found that severely worn tools could raise the cutting area's temperature by an average of 17.9 °C, directly linking tool wear to increased temperatures [3]. Queiroz and others observed significant wear and resultant bone tissue damage after 40 uses of a drill bit, analyzed through SEM monitoring and histological examination [4].

In 2020, Alam and colleagues investigated the impact of drill bit quality on bone drilling performance [5]. Their experimental results indicated a close correlation between drill bit wear and drilling cutting force, torque, temperature, and surface roughness. In 2021, Hu and his team studied the influence of crescent-textured parameters on the axial force during bone drilling [6]. They used a laser marker to create biomimetic crescent textures on the front cutting face of the drill bit. The findings showed that these biomimetic crescent textures significantly reduced the axial force during bone drilling, offering more stable axial force measurements and less stress fluctuation compared to traditional drill bits. In the same year, Shakouri and associates employed infrared thermography to study the drilling of bone materials, conducting experiments on bovine femur bones [7]. The results demonstrated that the temperature increase of the drill bit was directly related to the feed rate, whereas the temperature increase in the bone was inversely proportional to both the speed and feed rate. Amewoui and others developed a simplified analytical model in 2020 using a moving heat source method combined it with an image source approach, conducting studies with fresh pig femur bones [8]. This model successfully detailed the temperature rise during the drilling process.

As science and technology progress, research on the drilling process of bone materials has evolved from examining the effects of drilling parameters, tool geometrical parameters, and drilling conditions on drilling temperature, force, and post-drilling surface roughness, to applying various software for simulation analyses. Some scholars have also shifted their research focus to analyzing signals produced during the drilling process, indirectly monitoring the performance of bone material drilling.

Therefore, to mitigate the risks associated with severe tool wear—including elevated temperatures, bone damage, and tool failure—it is crucial to monitor tool wear during bone drilling. In 2019, Cao et al. [9] proposed a highly robust tool wear monitoring method by combining convolutional neural networks (CNN) with the derived wavelet framework (DWF). In 2020, Ambadekar et al. [10] utilized CNNs to monitor tool wear by using images of tools taken by microscopes during the machining process as input. They categorized tool wear into initial, moderate, and severe wear labels to train the CNN model. In 2021, Kumar et al. [11] designed a deep CNN architecture and adjusted various hyperparameters during the training process. Their results indicated that the model could extract features from both worn and unworn tools and classify them accurately. In 2022, Yao et al. [12] extracted local features from continuously collected sensor data to track tool condition and proposed a deep transfer reinforcement learning (DTRL) network based on long short-term memory (LSTM), dynamically adjusting the network size after training. In 2021, Liu et al. [13] utilized a TWM model based on a parallel residual stacked bidirectional LSTM network. This model could simultaneously extract spatiotemporal features of the original

signal and achieve multi-feature fusion through the residual network, resulting in high prediction accuracy. In 2020, An et al. [14] combined a CNN with stacked bidirectional and unidirectional LSTM networks (CNN-SBULSTM) for tool life prediction tasks by processing time series data. The results showed that the prediction accuracy could reach 90% without requiring expert knowledge weights. LSTM networks have strong applicability in tool wear monitoring and prediction.

This project aims to explore the impact of tool wear on bone drilling processes by establishing a monitoring system that collects force and vibration data during drilling. By labeling the extent of wear on the tool's cutting surface before each drilling session, a dataset on tool wear during bone drilling is constructed. A deep learning model is then developed to assess tool wear in real time, allowing timely tool replacement to reduce the risks of osteonecrosis and drill bit breakage during surgeries.

2. Wear Mechanism Analysis

Bone material is a finely engineered composite exhibiting anisotropy, as depicted in Figure 1. It primarily consists of two layers: cortical and trabecular bone. Cortical bone includes the osteon units, also known as the Haversian system, situated between the inner and outer circumferential lamellae [15]. These units are the fundamental structural components of the skeletal core. Trabecular bone, on the other hand, features a spongy structure located inside the inner circumferential lamellae. It is composed of numerous bone trabeculae interwoven into a sponge-like structure, offering a combination of porosity, strength, and lightness [16].

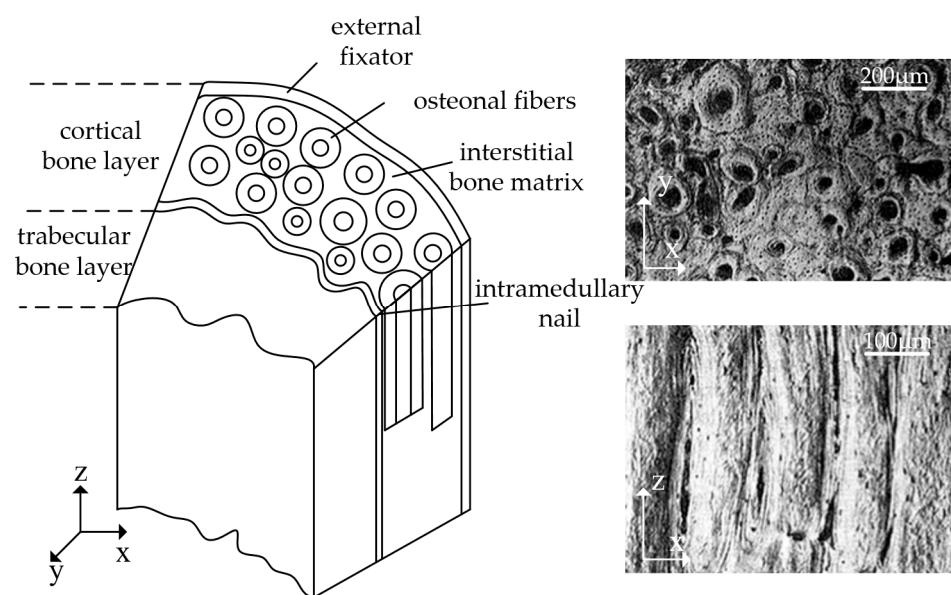


Figure 1. Bone material structure [15].

Tool wear is an inevitable occurrence during drilling processes, and bone material drilling is similar to metal drilling. When the tool comes into contact with the material, the material undergoes shearing due to the cutting action of the tool. The chips slide along the tool's rake face, generating significant amounts of energy and friction, which are then converted into heat, as illustrated in Figure 2. In practical drilling operations, intense friction and force arise from the contact between the tool's rake and flank faces with the bone material being drilled. This not only causes an increase in pressure and temperature of the bone material but also results in tool wear during the drilling process.

Additionally, during the bone drilling process, the cutting direction is not aligned with the osteons in cortical bone but instead cuts at periodic angles to the osteons. The elastic modulus of cortical bone material varies with these angles. Rellyi et al. [17] studied the elastic modulus of osteons at different angles.

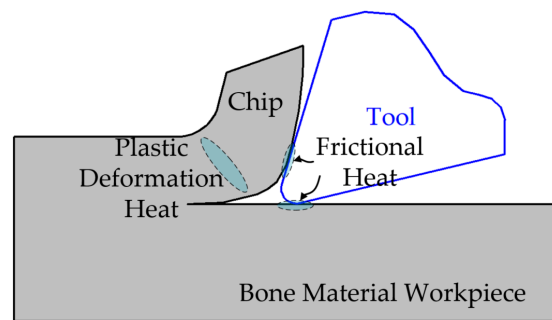


Figure 2. Drilling friction-producing area.

During the bone drilling process, common wear mechanisms include abrasion, adhesion, and oxidation. Abrasion occurs due to the relative motion between the drill bit and the bone tissue, leading to gradual material wear on the surface. Adhesion refers to the bonding between the drill bit material and the bone tissue, which not only increases the wear of the drill bit but may also degrade the quality of the drilled hole. Additionally, the frictional heat generated by the high-speed rotation of the drill bit in contact with bone tissue can cause oxidation reactions. The resulting oxides can further affect the performance of the drill bit and the integrity of the bone tissue.

Studies have shown that these wear mechanisms are prevalent during the bone drilling process. For example, Li et al. found that the use of ultrasonic-assisted bone drilling significantly reduces drill bit wear and adhesion [18]. Pourgivi et al. reported that ultrasonic-assisted drilling not only reduces oxidation reactions during drilling but also minimizes thermal damage to bone tissue [19]. Moreover, Akhbar and Sulong reviewed various drill bit designs and their effects on thermo-mechanical damage, emphasizing the importance of abrasion, adhesion, and oxidation in the bone drilling process [20].

Compared to other metal drilling materials, bone material may have lower hardness and density, but the drilling process cannot utilize effective cooling fluids. This inability prevents timely expulsion of bone chips from the hole. The bone chips, in contact with the continuously rotating drill bit, generate substantial friction. Moreover, as bone material is semi-brittle, flank wear becomes the predominant form of tool wear during the drilling process.

Flank wear can be measured using a microscope, and it is typically assessed by the flank wear width (V_B value) to determine whether the tool is in the initial, moderate, or severe wear stage. The international standard for tool bluntness employs the width of flank wear at the midpoint of the tool engagement. Therefore, this paper utilizes the V_B value to define the degree of wear [21].

2.1. Bone Material Cutting Mechanism

Since cortical bone in bone material is composed of osteons, which provide structural support through their fibrous arrangement, the drilling process involves rotational movement along the main axis and axial feed movement along the tool. The actual motion trajectory of the cutting edge is helical. During this process, the cutting edge can be conceptually divided into numerous infinitesimal segments engaging in orthogonal cutting.

In the drilling of cortical bone material, the orientation angle of the bone unit fibers relative to the main cutting edge, θ (ranging from 0° to 180°), significantly influences the cutting dynamics. As the cutting edge rotates along the main axis and advances axially, it traces a spiral cutting path. The parallel arrangement of the bone unit fibers means that changes in the angle between the cutting edge and the fibers significantly impact the cutting process and outcome, as shown in Figure 3. When θ is 0° or 180° , the cutting edge is parallel to the fiber direction, leading to compression and deformation of the bone tissue by the rake face of the tool. As the cutting edge progresses, the fibers in front bend and may eventually break, creating a “fiber extrusion” type of chip. Between 0° and 90° , both shearing and compressive forces act together to break the fibers, particularly near 0° where

the compressive force is more pronounced; near 90° , the shearing force dominates. At 90° , the cutting edge is perpendicular to the fibers, causing them to break due to shearing, resulting in chips with an oblique cut surface. Beyond 90° , the fibers are primarily subjected to pushing forces until the fiber angle reaches 90° , at which point the pushing force becomes dominant, defining the primary mode of cutting.

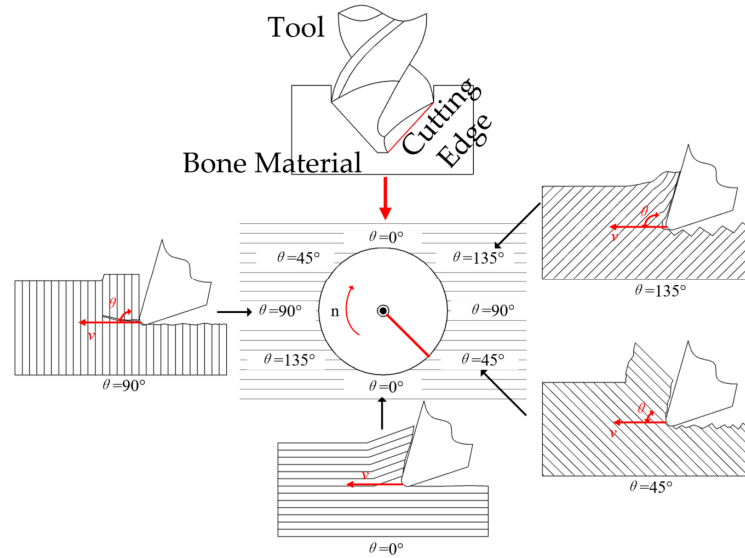


Figure 3. Fiber angle of different bone units in the drilling of bone materials.

2.2. Primary Cutting Edge Mechanical Model

During the bone drilling process, the use of medical-grade stainless steel for drill bits, which has a lower hardness compared to the tools used in metal material drilling, results in severe wear on the main cutting edges and the flank face [22].

The wear process alters the contour of the main cutting edges from a curved shape to a new shape. Therefore, the worn main cutting edges are simplified to an elliptical arc, as shown in Figure 4b. Based on geometric characteristics, the contact area between the worn main cutting edges and the bone material is divided into three parts: the rake face area 1, the area beneath the elliptical arc cutting edge 2, and the area beneath the flank face 3, as illustrated in Figure 5.

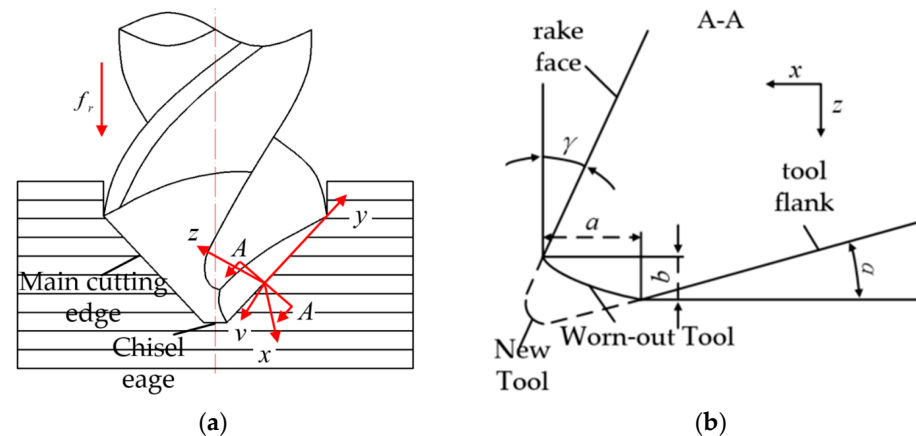


Figure 4. (a) Main cutting edge element. (b) Wear geometrical characteristics of main cutting edge element.

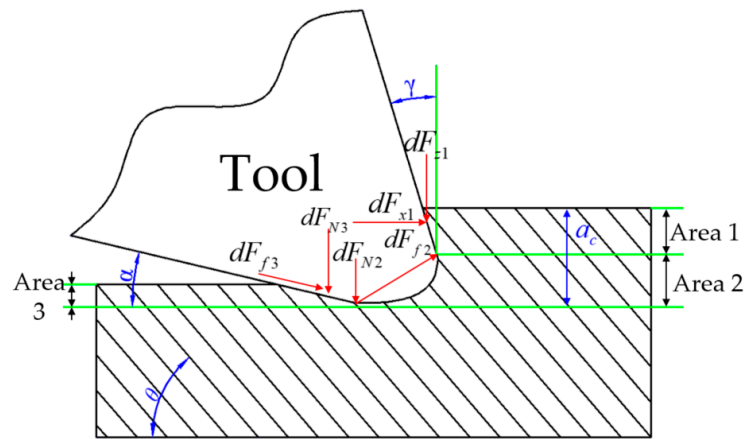


Figure 5. Cutting forces of worn main cutting edge element.

In Region 1 on the rake face, brittle fracture occurs at the cross-section of the bone unit fibers and the inter-bone plate matrix due to the shearing and compressive actions on the rake face, leading to the formation of chips. Since the rake face wear in bone drilling is typically not severe, the cutting force generated by the worn rake face is similar to that produced by a new rake face. Referring to the cutting force model for orthogonal cutting with a new tool, the basic cutting forces dF_{x1} and dF_{z1} along the x -axis and z -axis in Region 1 can be expressed as:

$$dF_{x1} = \tau_1 a_e \frac{\sin \phi \tan(\phi + \beta - \gamma) + \cos \phi}{\frac{\tau_1}{\tau_2} \cos(\theta - \phi) \sin \theta - \sin(\theta - \phi) \cos \theta} dl \tag{1}$$

$$dF_{z1} = \tau_1 a_e \frac{\cos \phi \tan(\phi + \beta - \gamma) - \sin \phi}{\frac{\tau_1}{\tau_2} \cos(\theta - \phi) \sin \theta - \sin(\theta - \phi) \cos \theta} dl \tag{2}$$

The subscript 1 in dF_{x1} and dF_{z1} denotes Region 1, τ_1 is the shear strength of the fibers, τ_2 is the shear strength of the matrix, γ is the rake angle of the tool, β is the friction angle between the chip and the rake face, ϕ is the shear plane angle, a_e is the cutting depth, dl is the length of the main cutting edge element, and θ is the fiber orientation angle.

Based on the geometric relationships in Figure 6, the fundamental cutting forces dF_{x1} and dF_{z1} in Region 1 can be further calculated as follows:

$$dF_{x1} = \tau_1 a_e \frac{\sin \phi \tan(\phi + \beta - \gamma) + \cos \phi}{\frac{\tau_1}{\tau_2} \cos(\theta - \phi) \sin \theta - \sin(\theta - \phi) \cos \theta} \frac{1}{\sin \delta} \frac{r}{\sqrt{r^2 - t^2}} dr \tag{3}$$

$$dF_{z1} = \tau_1 a_e \frac{\cos \phi \tan(\phi + \beta - \gamma) - \sin \phi}{\frac{\tau_1}{\tau_2} \cos(\theta - \phi) \sin \theta - \sin(\theta - \phi) \cos \theta} \frac{1}{\sin \delta} \frac{r}{\sqrt{r^2 - t^2}} dr \tag{4}$$

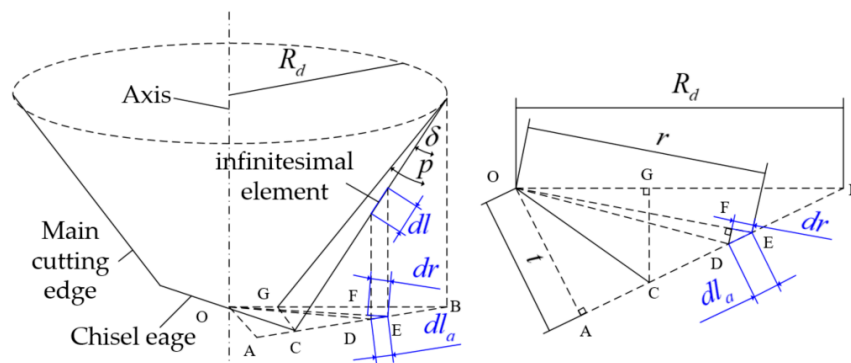


Figure 6. The relation between the element length dl and radius increment dr .

Due to the presence of a fiber angle θ between the bone unit fiber direction and the cutting speed during the cutting process, Figure 7 illustrates the variation of the fiber angle at different positions relative to the bone unit fiber along the main cutting edge. The fiber angle θ can be expressed as a function of the radial distance r .

$$\theta = \theta_0 + \arcsin \frac{t}{R_d} - \arcsin \frac{t}{r} \tag{5}$$

where θ_0 is the fiber angle when the radial distance r is equal to the drilling radius R_d .

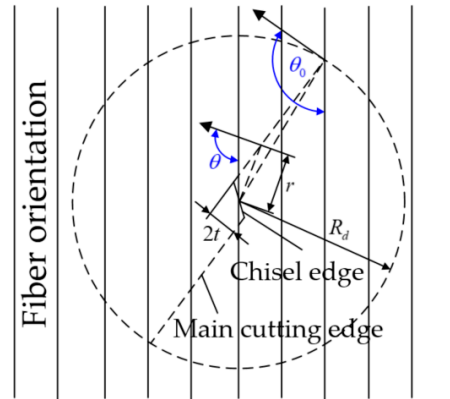


Figure 7. Skeletal unit fiber angle θ .

In Region 2, tool wear causes the cutting edge to become elliptical, thereby pushing the cutting material downward. Based on Hertzian contact theory and assuming a cylindrical model, the indentation depth is approximated as the length of the minor axis b of the workpiece. The normal force F_N derived from this can be related to Young’s modulus E_{\perp} perpendicular to the bone unit fiber direction and the average length of the minor axis \bar{b} . The expression for the normal force is as follows:

$$dF_N = \frac{1}{8} \pi E_2 \bar{b} \frac{1}{\sin \delta} \frac{r}{\sqrt{r^2 - t^2}} dr \tag{6}$$

where E_2 is the Young’s modulus of the bone material perpendicular to the bone unit fiber direction, and \bar{b} is the average length of the minor axis along the entire main cutting edge.

The friction force is controlled by the friction coefficient μ , $\Psi = \arctan(\bar{b}/a)$ and can be calculated based on the principles of tribology.

$$dF_{f2} = \mu dF_N \cos \Psi \tag{7}$$

Assuming the major axis a increases linearly with the radial distance r , the fundamental cutting forces along the x -axis and z -axis in Region 2 can be calculated as follows:

$$dF_{x2} = \frac{\pi}{8} \mu \cos^2 \Psi E_1 \bar{b} \frac{1}{\sin \delta} \frac{r}{\sqrt{r^2 - t^2}} dr \tag{8}$$

$$dF_{z2} = \frac{\pi}{8} (1 - \mu \sin \Psi \cos \Psi) E_1 \bar{b} \frac{1}{\sin \delta} \frac{r}{\sqrt{r^2 - t^2}} dr \tag{9}$$

In Region 3, the contact between the flank face and the cutting material surface is caused by the rebound of the cutting material. This process can be approximated as an elastic half-space contact based on Hertzian contact theory. Assuming that the rebound height is linearly related to the average minor axis length \bar{b} , the normal force dF_{N3} in the drilling Region 3 can be obtained from the following equation:

$$dF_{N3} = \frac{1}{2} K_3 E_2 \bar{b} \frac{1}{\sin \delta} \frac{r}{\sqrt{r^2 - t^2}} dr \tag{10}$$

where K_3 is the coefficient, the friction force dF_{f3} between the flank face and the machined surface is given by $dF_{f3} = \mu dF_{N3} \cos \alpha$, and α is the tool's relief angle.

Therefore, the fundamental cutting forces dF_{x3} and dF_{z3} along the x -axis and z -axis in Region 3 can be expressed as follows:

$$dF_{x3} = \frac{1}{2} K_3 \mu \cos^2 \alpha E_2 \bar{b} \frac{1}{\sin \delta} \frac{r}{\sqrt{r^2 - t^2}} dr \tag{11}$$

$$dF_{z3} = \frac{1}{2} K_3 (1 + \mu \sin \alpha \cos \alpha) E_2 \bar{b} \frac{1}{\sin \delta} \frac{r}{\sqrt{r^2 - t^2}} dr \tag{12}$$

By summing all the cutting forces from the three regions, the total cutting forces dF_x and dF_z along the x -axis and z -axis along the worn main cutting edge can be calculated as follows: $dF_x = dF_{x1} + dF_{x2} + dF_{x3}$, $dF_z = dF_{z1} + dF_{z2} + dF_{z3}$.

The cutting forces defined above are in the orthogonal coordinate system $x - y - z$, as shown in Figure 8. To obtain the vertical downward thrust generated by the drill bit, the cutting forces dF_x and dF_z are first resolved in the inclined coordinate system $x' - y' - z'$. Then, the resulting components $dF_{x'}$, $dF_{y'}$, and $dF_{z'}$ are resolved in the actual drilling coordinate system $x'' - y'' - z''$. Finally, by summing all the cutting forces along the z'' -axis, the axial force dF_{t1} generated by the drill bit during the drilling process can be expressed as:

$$dF_{t1} = dF_{y'-z''} + dF_{z'-z''} = \sin i \sin \tau dF_x + \cos \tau dF_z \tag{13}$$

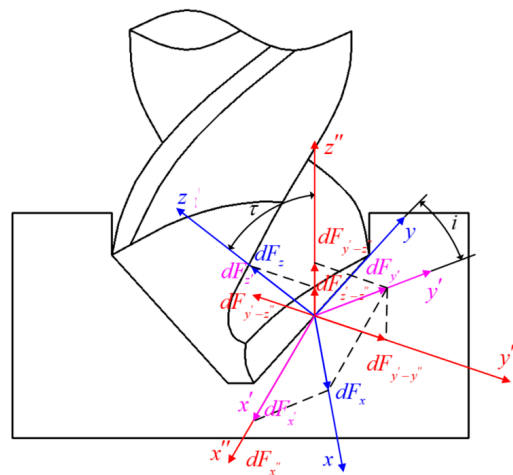


Figure 8. Schematic diagram of cutting force decomposition.

By integrating the thrust dF_{t1} of all the components, the thrust F_{t1} generated by the two main cutting edges can be expressed as:

$$F_{t1} = 2 \int_{t/\sin \varphi}^{R_t} dF_{t1} \tag{14}$$

where φ is the angle between the chisel edge and the main cutting edges.

The thrust generated by the chisel edge can be expressed as F_{t2} after a transformation:

$$F_{t2} = \int_{-t/\sin \varphi}^{t/\sin \varphi} \frac{E_3}{1 - \nu_{31}^2} \left(kt + \frac{f_r}{2} \right) \tan \gamma_w \cos \gamma_f dr \tag{15}$$

By superimposing the thrusts F_{t1} and F_{t2} of the main cutting edges and the chisel edge, respectively, the axial force F_t , considering the effect of wear, can be expressed as:

$$F_t = F_{t1} + F_{t2} \tag{16}$$

In summary, the feed rate, spindle speed, and geometric parameters of the tool significantly influence the axial force in drilling. Tool wear leads to the degradation of the

performance of the main cutting edges, thereby affecting the axial force, making it a reliable indicator for evaluating tool wear. As wear progresses, not only does the axial force change, but the forces in the horizontal direction also vary accordingly [23]. Therefore, an effective monitoring strategy should include an analysis of the changes in horizontal forces. Due to the periodic variation of the unit fiber angle during the drilling process, performing time–frequency domain analysis on the collected signals is a feasible method for monitoring tool wear in the drilling process of bone materials.

3. Materials and Methods

The experimental setup is illustrated below, conducted on a multifunctional CNC machine (JET-3000). The CNC milling machine (model: SIEG JET3000) is manufactured by Shanghai SIEG Machinery Co., Ltd., located in Shanghai, China. A medical orthopedic drill bit with a diameter of 3 mm was used to perform ex vivo studies on well-conditioned fresh bovine femur bones. In this study, standard medical twist drills were used, as shown in Figure 9a. The geometric parameters are listed in Table 2. The parameters of the tool materials are presented in Table 3.

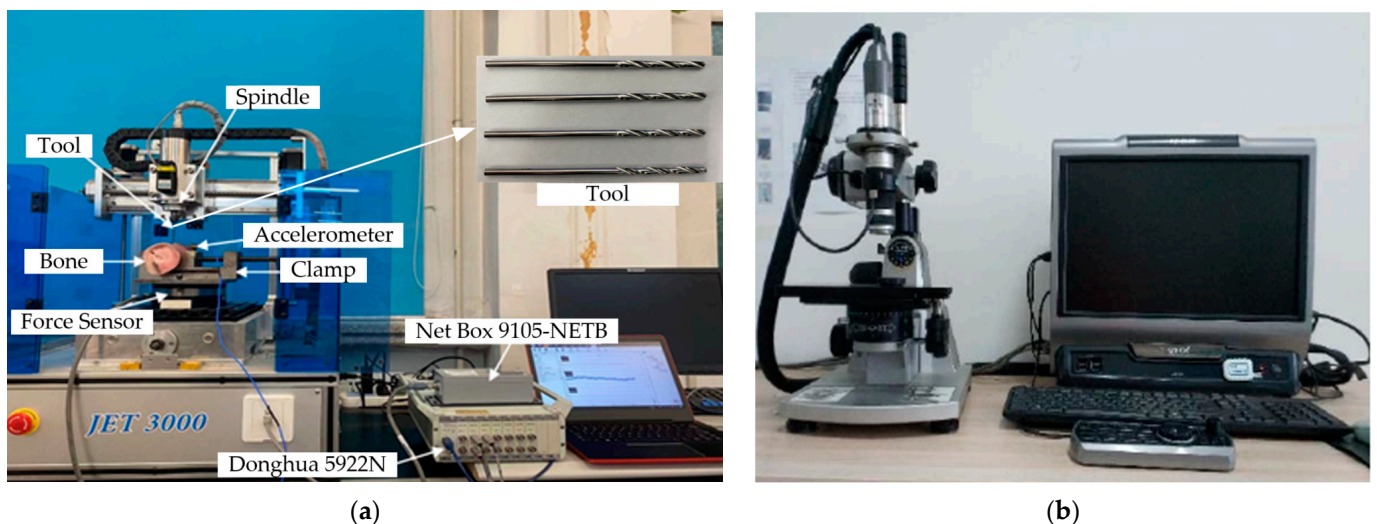


Figure 9. (a) Experimental platform for data collection and condition monitoring of bone material drilling process. (b) Super-depth-of-field microscope.

Table 2. Tool geometry.

Tool Diameter/mm	l /mm	L /mm	Apex Angle	Helix Angle	Chisel Edge Angle
3	140	55	118°	25°	55°

Table 3. Tool material parameters.

Ingredient	C	Si	Mn	S	P	Cr	Ni
content	0.36–0.45	≤ 0.80	≤ 0.80	≤ 0.03	≤ 0.40	12–14	≤ 0.60

Prior to the experiment, the surface of the bone material was cleaned of soft tissues, and the bone used was the more uniform and regular middle section of the femur, from which both ends had been sawn off. The bone marrow was removed, and the bone was repeatedly washed with a saline solution to ensure that no residual soft tissues remained on the surface.

The utilized tool condition monitoring system included an Omega160 multi-axis force/torque sensor, a PCB accelerometer, and a Net Box 9105-NETB charge amplifier,

along with a Donghua DH5922N, to collect force and vibration signals. Among the equipment used, the Omega160 multi-axis force/torque sensor and the Net Box 9105-NETB are manufactured by ATI Industrial Automation, Inc., located in Apex, NC, USA. The Donghua DH5922N is produced by Jiangsu Donghua Testing Technology Co., Ltd, based in Jingjiang, China. During the experiments, the fixture was mounted above the dynamometer, and the accelerometer was attached as close as possible to the clamp holding the bone material to minimize interference and capture more accurate signals.

Tool wear was assessed using a VHX-1000 type super-depth-of-field microscope, with the degree of wear quantified by the flank wear width VB value. The VHX-1000 super-depth-of-field microscope is manufactured by KEYENCE Corporation, headquartered in Osaka, Japan. Tool wear was categorized based on the VB value: $VB < 80 \mu\text{m}$ indicated initial wear; $80 \mu\text{m} \leq VB \leq 140 \mu\text{m}$ indicated moderate wear; and $VB > 140 \mu\text{m}$ indicated severe wear [24]. Before the start of drilling, the wear on the flank face of the tool was measured using a super-depth-of-field microscope. The measurements were taken three times, and the average value was used to reflect the current tool wear condition during the drilling process. The VHX-1000 super-depth-of-field microscope, as shown in Figure 9b, was used to measure the wear on the flank face of the tool after wear, as depicted in Figure 10.

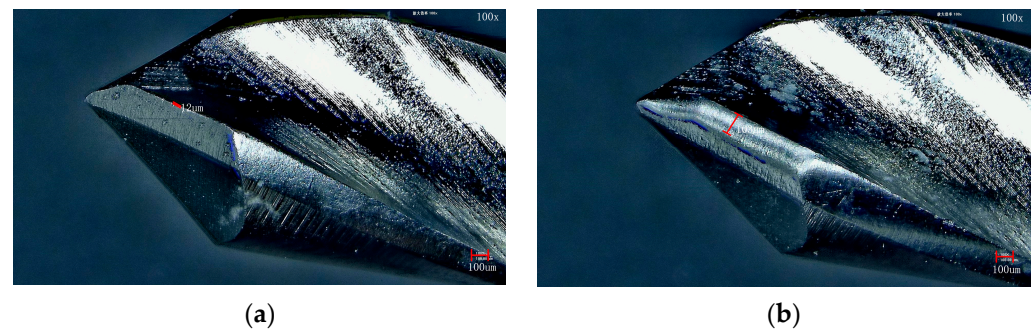


Figure 10. Inspection picture of rear tool face wear. (a) Unworn tool; (b) worn tool.

This study conducted two rounds of wear experiments: the first aimed to determine the optimal drilling parameters within the typical range for conventional orthopedic surgery, ensuring that issues such as bone fracturing were avoided, and to prepare for the creation of a comprehensive tool wear dataset. The second round of experiments was based on the parameters established in the first round. It involved collecting three-dimensional force signals and vibration signals throughout the entire lifecycle of the tool and measuring the tool wear, averaging three measurements to correspond with the sensor signals and to preserve the data, thereby constructing a complete dataset of the tool wear process. The experimental parameters were referenced from those of medical handheld bone drills and their processing conditions to accurately simulate real clinical orthopedic surgery signals. The detailed experimental scheme is presented in Table 4.

Table 4. Experimental scheme for drilling of bone materials.

Feed Rate (mm/min)	Spindle Speed 1 (r/min)	Spindle Speed 2 (r/min)	Spindle Speed 3 (r/min)	Spindle Speed 4 (r/min)	Spindle Speed 5 (r/min)
30	1000	1250	1500	1750	2000
40	1000	1250	1500	1750	2000
50	1000	1250	1500	1750	2000
60	1000	1250	1500	1750	2000

4. Results and Discussion

Figure 11a illustrates the changes in the Z-direction force during the bone drilling process under conditions of a 3 mm diameter, a rotational speed of 1500 rpm, and a feed rate of 50 mm/min. Bone drilling can be divided into five stages: initially, there is no drilling force; as the tool contacts the bone material, the drilling force increases; when the cutting edge is fully engaged, the force reaches a maximum stable value (approximately 25 N) with fluctuations; the force decreases as the chisel edge exits; and finally, the tool completely withdraws [25]. As shown in Figure 11b, the experiment demonstrated that higher spindle speeds resulted in lower drilling forces, while higher feed rates increased the drilling force [26]. Taking into account the practical aspects of surgery and drilling efficiency, the optimal parameters were selected as 1500 rpm for the spindle speed and 50 mm/min for the feed rate [27].

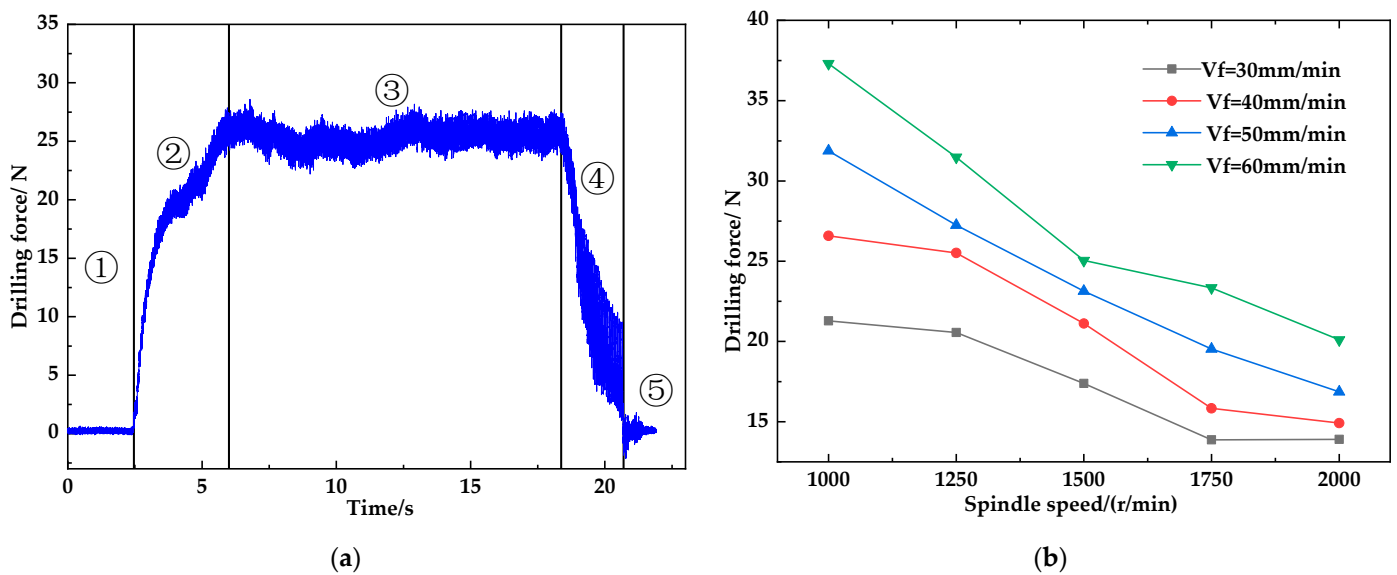


Figure 11. Drilling force. (a) Drilling force in Z direction of the original signal. (b) Drilling force at different speeds and feed speeds.

Figure 12 shows the changes in vibration signals during the drilling process, divided into five stages, similar to the force signals: In the initial stage, the bone material is in a pre-machining state, and the vibration signal is weak, originating from the rotation of the spindle. In the second stage, as the tool begins drilling, the vibration signal intensifies. In the third stage, as the main cutting edge fully enters the bone material, the vibration signal stabilizes. In the fourth stage, as the drill bit exits the bone material, vibration increases due to the unevenness of the exit direction and tissue hardness, which might exacerbate the vibrations. In the final stage, after the tool withdraws, the vibrations decrease to the level of the spindle rotation. This vibration analysis is crucial for understanding the dynamics of bone drilling and optimizing surgical operations [28].

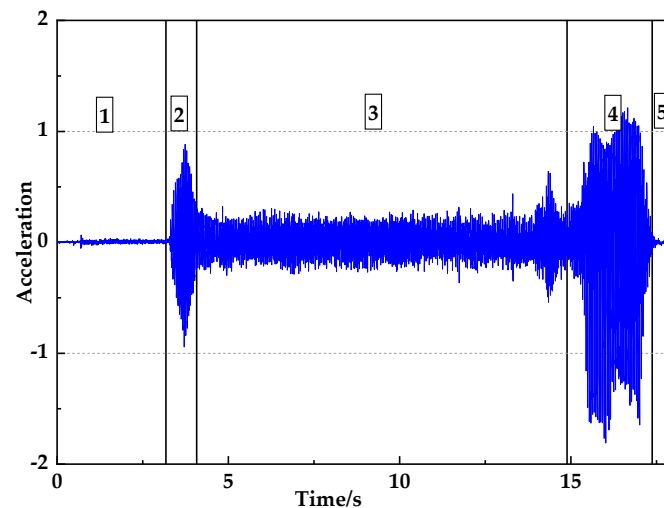


Figure 12. Original Z direction vibration signal.

4.1. Preprocessing

Due to the presence of noise and other redundant factors in the signals collected during the experiment, it is challenging to establish a clear relationship between the raw signals and the tool wear state or drilling depth. Thus, it is necessary to perform feature extraction and feature selection in the time domain, frequency domain, and time–frequency domain.

The signals from the third stage of the drilling process were selected, where the main cutting edge was fully engaged in the bone material and the drilling force reached its maximum value under normal conditions and stabilizes. This phase provided stable measurement signals, representing the actual drilling force under the current tool wear state. Therefore, all collected signals were filtered based on whether there was a sudden change in the Z-direction force signal, ultimately yielding 130 sets of drilling data. Additionally, the time when the drilling entered the third phase was determined based on the Z-direction force signal, as shown in Figure 13.

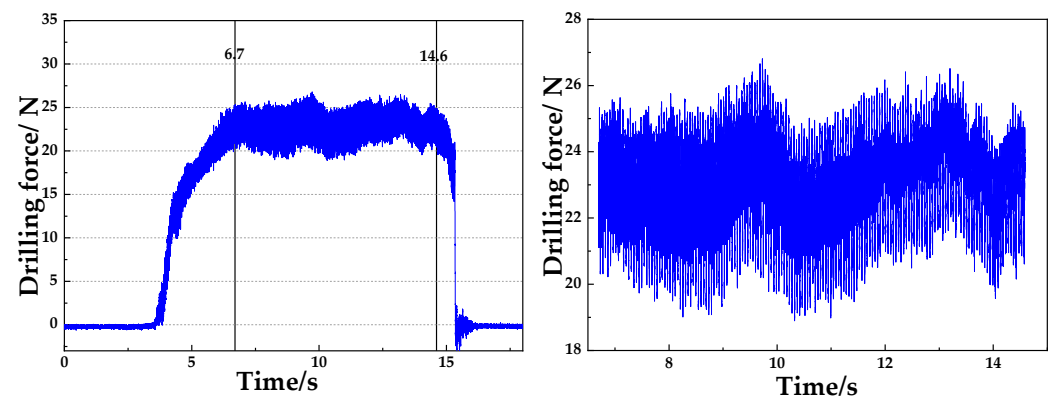


Figure 13. Determine the time of stable drilling state.

Based on the time segment of the stable drilling state, the collected raw data were processed. The triaxial drilling force signals and vibration signals were extracted according to the determined time segments. For example, the Z-direction vibration signal was extracted according to the time segment when the drilling process entered a stable state, as illustrated in Figure 14.

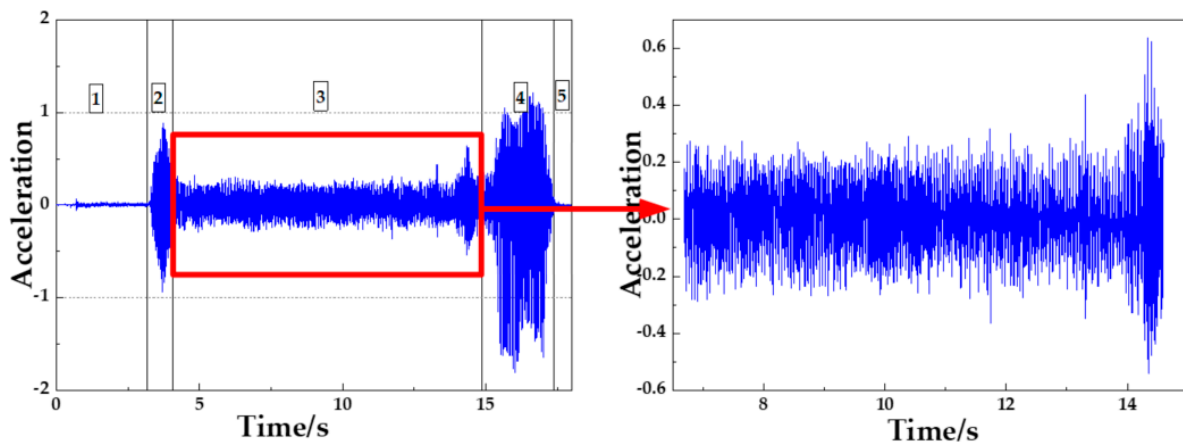


Figure 14. Z-direction vibration signal extraction in stable drilling state.

4.2. Feature Extraction

Time-domain features provide an intuitive representation of the characteristics of force and vibration signals under the current drilling state. These features include both dimensional and non-dimensional characteristics, which reflect the signal’s temporal variation. Six channels of time-domain features were extracted, and the specific indices of the extracted features are listed in Table 5. Due to the inevitable influence of environmental and processing noise on the time-domain signals collected during the drilling process, a frequency-domain analysis was conducted to more accurately analyze the collected signals.

Table 5. Time-domain characteristic index.

Characteristic Indicators	Calculation Formula	Characteristic Indicators	Calculation Formula
Mean value	$\bar{X} = \frac{1}{N} \sum_{i=1}^n x_i$	Waveform Factor	$S = \frac{X_{rms}}{\frac{1}{N} \sum_{i=1}^N x_i }$
Peak value	$X_{peak} = \max(x_i)$	Impulse factor	$I = \frac{X_{peak}}{\frac{1}{N} \sum_{i=1}^N x_i }$
Root mean square value	$X_{rms} = \sqrt{\frac{1}{N} \sum_{i=1}^N x_i^2}$	Skewness factor	$K_3 = \frac{\frac{1}{N} \sum_{i=1}^N (x_i - \bar{x})^3}{X_{rms}^3}$
Root amplitude	$X_r = \left(\frac{1}{N} \sum_{i=1}^N \sqrt{ x_i } \right)^2$	Crest factor	$C = \frac{X_{peak}}{X_{rms}}$
Skewness value	$C_s = \frac{1}{N} \sum_{i=1}^N \left(\frac{x_i - \bar{x}}{\sigma} \right)^3$	Margin Factor	$L = \frac{X_{peak}}{\left(\frac{1}{N} \sum_{i=1}^N \sqrt{ x_i } \right)^2}$
Kurtosis value	$\beta = \sqrt{\frac{1}{N} \sum_{i=1}^N (x_i - \bar{x})^4}$	Kurtosis Factor	$K = \left[\sqrt{\frac{1}{N} \sum_{i=1}^N (x_i - \bar{x})^4} \right] / \left\{ \left[\frac{1}{N} \sum_{i=1}^N (x_i - \bar{x})^2 \right]^2 \right\}$

Frequency-domain feature extraction requires performing a Fast Fourier Transform (FFT) on the signals. Since the signals collected by the sensors were discrete values, a one-dimensional N-point Discrete Fourier Transform (DFT) was initially performed. The six channels of signals were then subjected to frequency-domain feature extraction, with specific feature indices detailed in Table 6 [29].

In the context of bone material drilling, the signals collected cannot be adequately characterized using solely time-domain or frequency-domain parameters. It is essential to integrate both time and frequency domain information for a comprehensive analysis of the signals.

Table 6. Frequency domain characteristic index.

Characteristic Indicators	Calculation Formula
Center of Gravity Frequency	$FC = \frac{\int_0^{+\infty} fP(f)df}{\int_0^{+\infty} P(f)df}$
Mean square frequency	$MSF = \frac{\int_0^{+\infty} f^2P(f)df}{\int_0^{+\infty} P(f)df}$
Root mean square frequency	$RMSF = \sqrt{MSF}$
Frequency variance	$VF = \frac{\int_0^{+\infty} (f-FC)^2P(f)df}{\int_0^{+\infty} P(f)df}$

This paper employed wavelet packet analysis technology to extract frequency domain characteristics from the signals, dividing the frequency bands into multiple levels. This technique allows for further decomposition of the wavelet space, specifically decomposing the undivided multi-resolution high-frequency bands further. According to practical engineering requirements, the collected signals can be segmented into multiple layers, thereby enhancing the time–frequency resolution capability. This approach proves more effective than conventional wavelet analysis and offers broader application value. It also facilitates a more detailed segmentation of the time domain, making it easier to analyze signals during the bone drilling process [30].

As shown in Figure 15, a three-layer wavelet packet analysis was demonstrated with an example where $L = 3$. This spatial division into three levels represents a detailed decomposition of the signal’s space using wavelet packets.

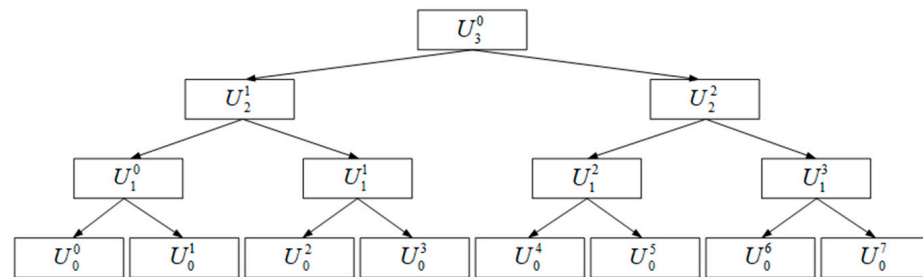


Figure 15. Spatial subdivision of three-layer wavelet packet analysis.

During the wavelet packet decomposition process, the higher the level of decomposition, denoted as L , the lower the resolution of the coefficient space and the larger the scale. This feature enables more effective time–frequency localization analysis of signals containing a significant amount of mid-to-high frequency information.

Let the wavelet packet coefficients on subspaces $U_j^{2^n}$ and $U_j^{2^{n+1}}$ be denoted as $d_j^{2^n}$ and $d_j^{2^{n+1}}$, respectively. Based on the definition of wavelet packets, the following fast decomposition and reconstruction algorithm can be derived:

Wavelet Packet Decomposition Algorithm:

$$\begin{cases} d_j^{2^n}[k] = \sum_{l \in \mathbb{Z}} h_{l-2k} d_{j+1}^n[l] \\ d_j^{2^{n+1}}[k] = \sum_{l \in \mathbb{Z}} g_{l-2k} d_{j+1}^n[l] \end{cases} \tag{17}$$

Wavelet Packet Reconstruction Algorithm:

$$d_{j+1}^n = \sum_{k \in \mathbb{Z}} h_{k-2l} d_j^{2^n}[l] + \sum_{k \in \mathbb{Z}} g_{k-2l} d_j^{2^{n+1}}[l] \tag{18}$$

Wavelet packet transforms are particularly adept at analyzing high-frequency components. They are highly effective for time–frequency localized analysis when the received signals contain a significant amount of high-frequency information. As tool wear in the

drilling process intensifies, it can be reflected by changes in the frequency of the signal. Initially, a three-level wavelet packet decomposition was applied to decompose and reconstruct the signals collected from six sensors. Taking one of these channels as an example, with a signal length of 10,000 points, the three-level wavelet packet decomposition and reconstruction yielded time-domain images of eight sub-bands, as shown in Figure 16. By calculating the energy of the wavelet packet coefficients, the energy ratios within different frequency bands varied with the degree of tool wear, ultimately saving the energy ratio of the eight bands as time–frequency domain features. The energy proportion of each band under different degrees of tool wear is depicted in Figure 17. Under varying degrees of wear, the energy proportion in each band differed after wavelet packet decomposition; comparing initial wear to severe wear, there was a noticeable decrease in the wavelet packet energy proportion in bands 1, 2, 3, 7, and 8, while a significant increase was observed in bands 4 and 5.

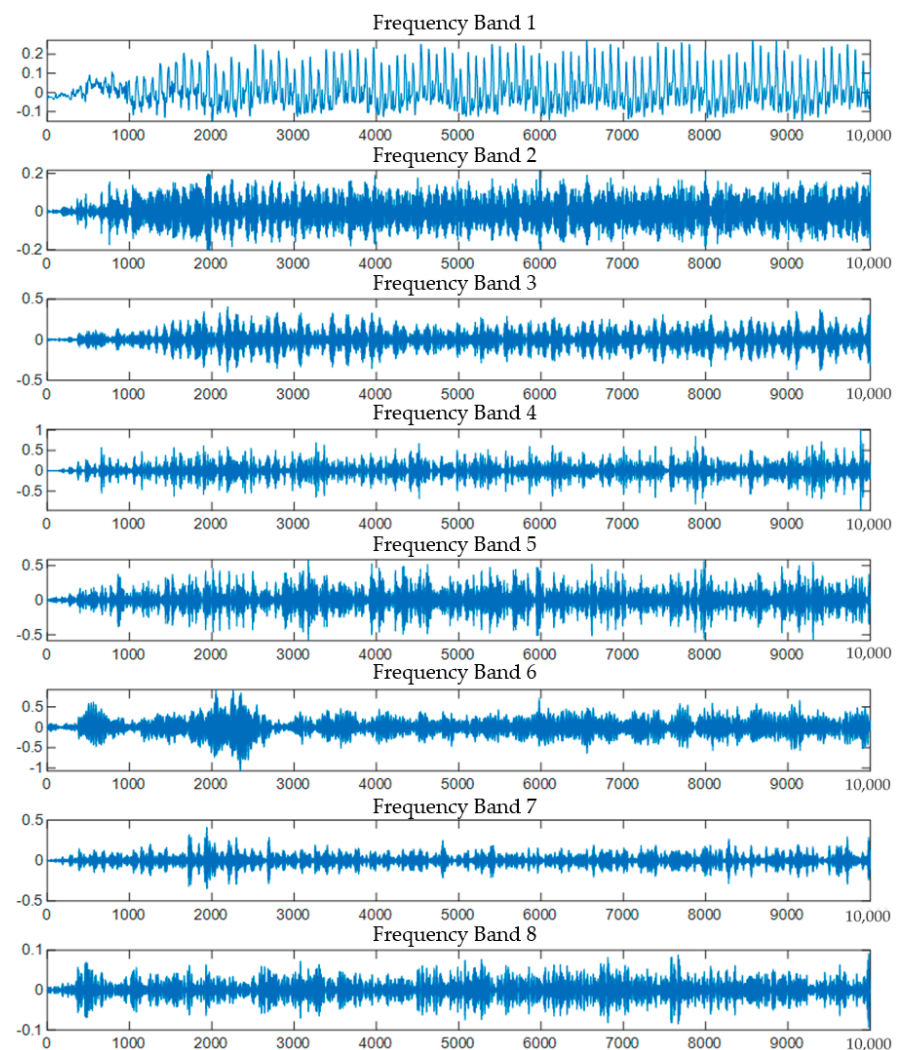


Figure 16. Sub-band time-domain image.

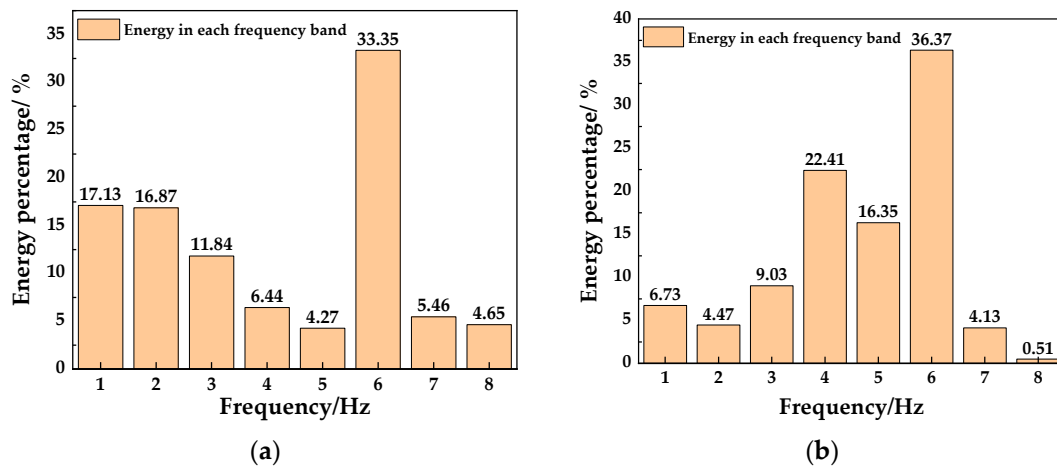


Figure 17. Proportion of energy in each sub-band: (a) initial wear; (b) moderate wear.

4.3. Feature Analysis Based on Pearson Correlation Coefficient

The Pearson correlation coefficient measures the degree of linear correlation between features. All extracted features were analyzed based on their correlation, and feature selection was performed according to the results of this analysis. For deep learning models, excessive correlation can lead to biases in weight allocation during the training process, as the model tends to sample from highly correlated features, making the model dependent on these features and reducing its generalization ability. Therefore, it is advisable to avoid excessive correlation among features. If the Pearson correlation coefficient between features reaches 0.99 or 1, these features should be removed. Assuming we have features x and y , their Pearson correlation coefficient can be calculated using the following formula:

$$\rho_{x,y} = \frac{\text{cov}(x,y)}{\sigma_x\sigma_y} = \frac{E[(x - \mu_x)(y - \mu_y)]}{\sigma_x\sigma_y} \tag{19}$$

In this context, $\rho_{x,y}$ represents the Pearson correlation coefficient, cov represents covariance, σ represents the standard deviation, and E and μ represent the mathematical expectation.

Based on the calculations performed, the Pearson correlation coefficients are shown in Table 7. This article involves extracting 12 time-domain features, 4 frequency-domain features, and 8 time–frequency domain features from each of the 6 channels, resulting in a total of 144-dimensional features. For example, considering all 24 features extracted from the x-direction force signal, the Pearson correlation coefficients were calculated and are displayed in Figure 18 as a heatmap without displaying specific numerical values due to the large number of data points.

Table 7. Degree of relevance.

Correlation Coefficient	0–0.2	0.2–0.4	0.4–0.6	0.6–0.8	0.8–1.0
Correlation coefficient	Very weak or no correlation	Weak correlation	Moderately relevant	Strong correlation	Extremely strongly correlated

By utilizing Pearson correlation coefficient analysis, all features were evaluated to select those suitable for training deep learning models. Features with strong correlations were removed to reduce the dimensionality of the feature set and conserve memory during the model training process. Since the Pearson correlation coefficient only captures linear relationships, features with low correlation coefficients were retained. From the integrated analysis of the images, it was found that in the three-directional drilling force signal features, both the mean squared frequency and the root mean square frequency, as well as the root amplitude and the root mean square value, had correlations of 0.99. Similarly, in the

features of the three-directional vibration signals, the mean squared frequency showed a 0.99 correlation with the root mean square frequency. Due to the high degree of correlation, the root mean square frequency and root amplitude were removed from the drilling force signal features, and the root mean square frequency was also removed from the vibration signal features, leaving a total of 135 dimensions of features remaining.

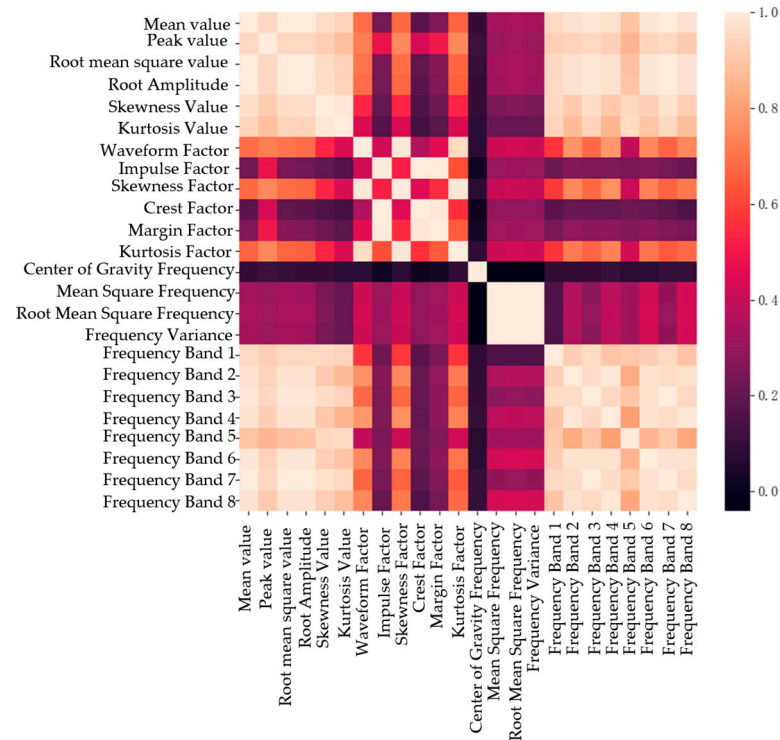


Figure 18. Pearson correlation coefficient thermodynamic diagram.

4.4. An ABI-LSTM Network Model Optimized with a Multi-Head Attention Mechanism

As depicted in Figure 19, the model proposed in this paper consists of a BI-LSTM layer, an attention mechanism module, and a fully connected classification layer. The ABI-LSTM network inputs data derived from feature extraction performed on cutting force and vibration signal data collected during the machining process. The labels were categorized according to the degree of wear on the drill bit's flank: initial wear, moderate wear, and severe wear. The dataset comprised 130 samples split into 60% for training, 20% for validation, and 20% for testing. Initially, the features were processed through the BI-LSTM network, then fed into the attention mechanism module, and finally, the predictions were mapped out through a fully connected layer to output the final tool wear prediction results. The discrepancy between the model's output categories and the actual classifications was measured using Cross Entropy Loss (CE loss), and the Adam optimization algorithm was used to update the weights during the model training process.

To enhance the generalization ability of the model, it was necessary to standardize the data before feeding it into the model. This paper employed the Z-score method for data standardization.

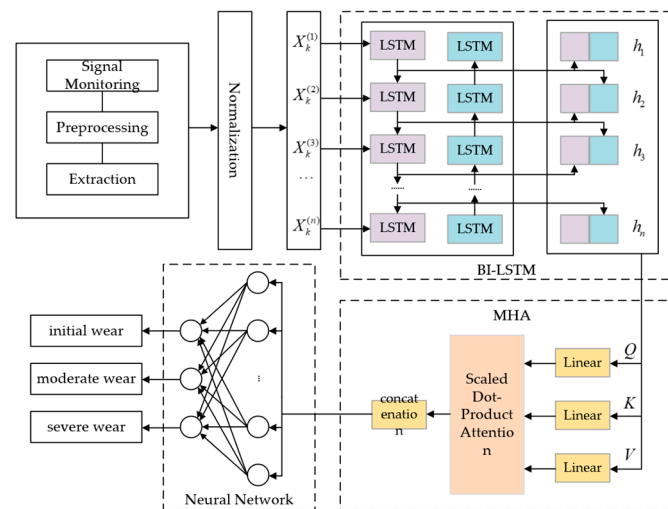


Figure 19. ABI-LSTM network structure.

4.5. Model Performance under Different Hyperparameters

During the experimental validation process based on the ABI-LSTM for classifying tool wear in the bone material drilling process, the primary focus was on adjusting the model’s hyperparameters. These adjustments included tuning the learning rate, the number of nodes in the hidden layers (hidden_size), the number of hidden layers (num_layers), and the Dropout ratio.

Selecting an appropriate learning rate is one of the key factors in optimizing model performance. The learning rate determines the speed at which the model parameters are updated. A learning rate that is too low may lead to a slow training process, while a learning rate that is too high can make the training process unstable, causing fluctuations in the loss function or even divergence. In this experiment, five learning rates were tested: 0.001, 0.002, 0.004, 0.006, and 0.008. With a fixed number of training iterations, it was observed that the network did not fully learn the features when the learning rate was set between 0.001 and 0.004; at a learning rate of 0.008, overfitting occurred, leading to reduced accuracy. The experimental results are presented in Table 8.

Table 8. Influence of different learning rates on model prediction results.

Learning Rate	Training Set Accuracy	Verify Set Accuracy	Test Set Accuracy
0.001	0.6893	0.6190	0.5769
0.002	0.7961	0.7142	0.6153
0.004	0.8640	0.8571	0.8076
0.006	0.9223	0.9047	0.8846
0.008	0.8834	0.7619	0.6538

As indicated by Table 9, the optimal performance of the model was achieved when the number of nodes in the hidden layer was 3. As the number of nodes in the hidden layer increased from 1 to 3, the accuracy on the test set also increased, suggesting that with fewer nodes, the model was unable to effectively learn the features in the training set. When the number of nodes in the hidden layer increased from 3 to 5, the accuracy on the training set continues to rise, but the accuracy on the test set decreased, indicating that overfitting occurred during the training process. After establishing the optimal number of nodes in the hidden layers, adjustments were made to the number of hidden layers, with results shown in Table 10. When the model had 32 nodes per hidden layer and 3 hidden layers, it achieved better training outcomes. This configuration balanced complexity and learning capability, effectively preventing overfitting while maintaining good generalization on unseen data.

Table 9. Influence of node number of different hidden layers on model prediction results.

The Number of Hidden Layer Nodes	Test Set Accuracy	Verify Set Accuracy	Test Set Accuracy
4	0.8737	0.8016	0.7692
8	0.8932	0.8354	0.8076
16	0.9223	0.9047	0.8461
32	0.9320	0.9223	0.8846
64	0.7766	0.6425	0.5769

Table 10. Influence of different hidden layers on model prediction results.

Hide the Number of Layers	Training Set Accuracy	Verify Set Accuracy	Test Set Accuracy
1	0.9320	0.9223	0.9230
2	0.9417	0.9365	0.9498
3	0.9611	0.9472	0.9615
4	0.9029	0.8095	0.7307
5	0.7669	0.6685	0.5384

During the Dropout process, randomly eliminating neurons with each training iteration results in a different network structure each time, forcing neurons to learn randomly. This approach helps avoid dependency on specific neurons during the training process, enabling the network to more effectively learn general data features. This increases the network's robustness and generalization capabilities, reduces training time, and minimizes the occurrence of overfitting. The impact of Dropout on the model was evaluated under different numbers of nodes in the hidden layers, all with three hidden layers. It was determined that a Dropout ratio of 0.4 was optimal. The final parameters for the ABI-LSTM network are detailed in Table 11.

Table 11. ABI-LSTM network parameter settings.

Parameter	Numeric Value and Type	Parameter	Numeric Value and Type
Learning rate	0.006	Optimize functions	Adam
Hide the number of layers	3	Batch_size	64
Hidden layer neurons	32	Epoch	200
The number of heads of the attention mechanism	4	Dropout	0.4
Loss function	CELoss	Number of classification categories	3

4.6. Comparison of Different Models

This paper compares the proposed improved ABI-LSTM tool wear prediction classification model with machine learning and other network models. Figure 20 visually displays the accuracy of the SVR, CNN, RNN, and ABI-LSTM models in classification results. Additionally, the confusion matrix reveals the probability of misclassification in the three categories of initial wear, moderate wear, and severe wear.

Under the category of initial wear, all four models exhibited high precision with prediction probabilities reaching 100%. However, for the true condition of moderate wear, the SVR model predicted 21% as initial wear and 14% as severe wear, while the CNN and RNN predicted 21% as initial wear. In the case of severe wear, SVR predicted 20% as moderate wear and 14% as moderate wear again, the CNN predicted 30% as moderate wear, and the RNN predicted 20% as moderate wear. In contrast, the ABI-LSTM model, under the true condition of moderate wear, only misclassified 7% as initial wear and 7% as severe wear, indicating superior classification performance.

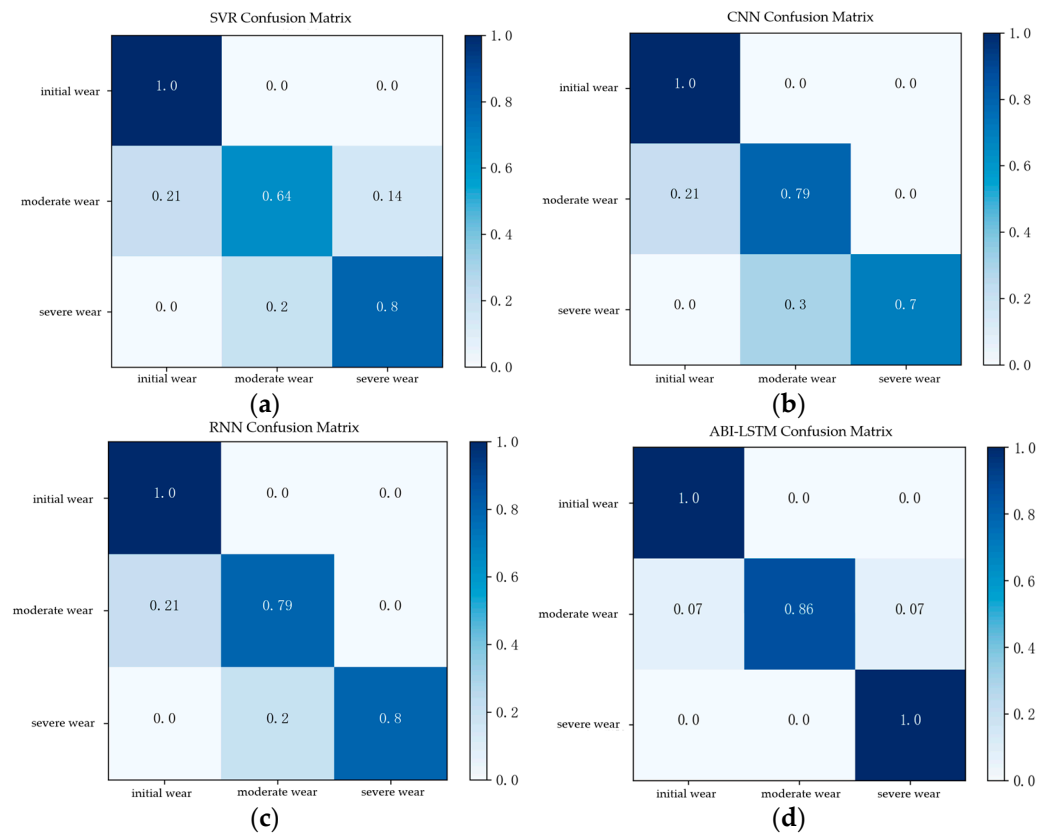


Figure 20. Confusion matrix of different network structures; (a) SVR confusion matrix; (b) CNN confusion matrix; (c) RNN confusion matrix; (d) ABI-LSTM confusion matrix.

Considering the classification of tool wear states during bone material drilling processes, it is crucial to avoid situations where the tool is severely worn during surgery. SVR, CNN, and RNN models tended to misclassify severely worn tools as moderately worn, performing worse compared to ABI-LSTM.

ROC (receiver operating characteristic) curves for the SVR, CNN, RNN, and ABI-LSTM models were plotted to depict their predictive performances. The steeper and higher the ROC curve, the better the model performance. ABI-LSTM's appeared steeper and closer to point (0,1), as shown in Figure 21.

Building on the ROC curves, the Area Under the Curve (AUC) was calculated and graphically represented in Figure 22, which distinctly shows the accuracy of each model under different classification conditions. In the categories of moderate and severe wear, ABI-LSTM consistently exhibited superior performance.

In conclusion, based on the analysis presented, considering the time-dependent and spatial-dependent characteristics of tool wear in the bone material drilling process, the ABI-LSTM model utilizing "memory gates" and a multi-head attention mechanism for feature selection achieved better classification results in a three-category setup. Not only did it maintain higher overall accuracy than other methods did, but it also ensured that severely worn tools were not misclassified as moderately worn in actual surgical scenarios. ABI-LSTM's minimal misclassification of severely worn tools demonstrated its absolute advantage in the classification problem addressed in this paper, making it more suitable for monitoring tool wear in bone material drilling processes.

Based on the tool wear classification model constructed for the bone material drilling process, this paper aimed to achieve real-time monitoring of various parameters during the drilling process, save monitoring signals, and track features of the drilling operation. To facilitate these capabilities, a bone material drilling status monitoring system was developed using Matlab App Designer. This system allows for the viewing and saving of information

regarding the machine tool, sensors, and tool wear status. The system includes several interfaces: a sensor initialization interface, a sensor signal monitoring interface, a signal feature analysis interface, and a bone material drilling process monitoring interface. The interface for monitoring the state of the bone material drilling process is shown in Figure 23. During the drilling process, this system monitors the degree of tool wear, machine tool parameters, and the operational status of sensors. Signals generated during the drilling process are collected by sensors, and after feature extraction and selection, they are fed into a deep learning model. The trained model is then used to identify the current level of tool wear during the drilling process. The system displays the state of tool wear and issues an alert when the drill bit is operating in a severely worn condition. This system, based on the ABI-LSTM deep learning model, enables the functionality of monitoring the degree of tool wear during the bone material drilling process.

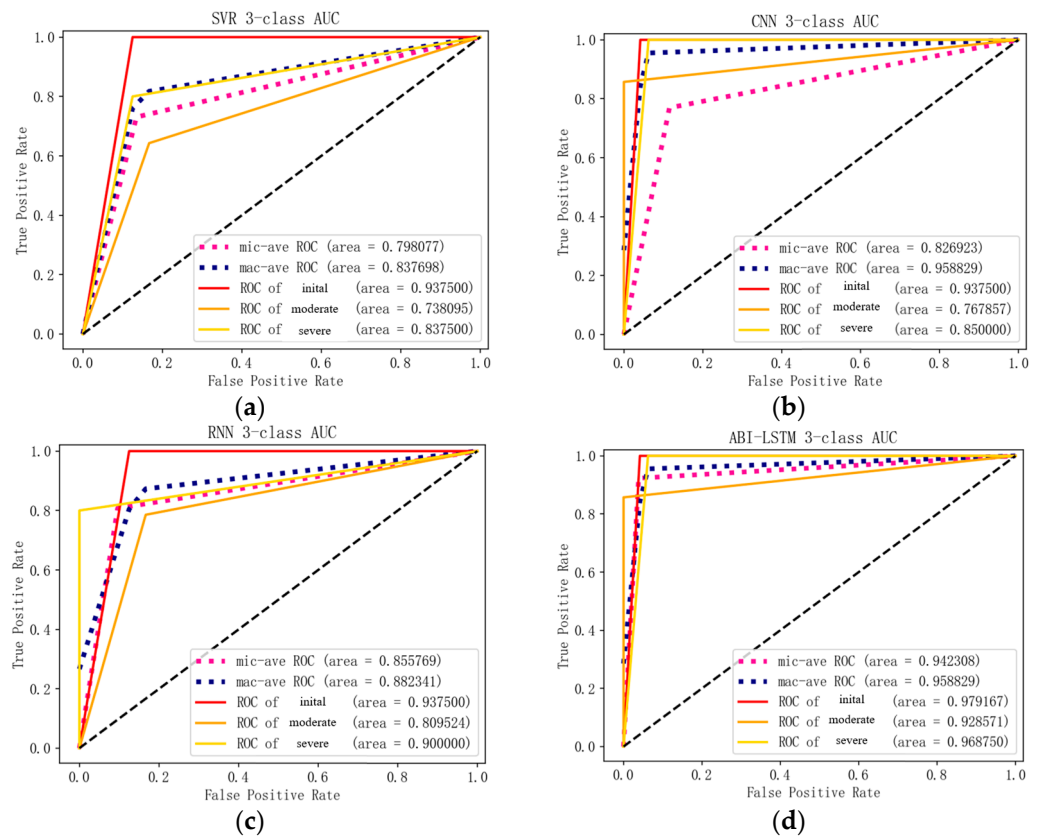


Figure 21. ROC curve of different network structures: (a) SVR’s ROC curve; (b) CNN’s ROC curve; (c) RNN’s ROC curve; (d) ABI-LSTM’s ROC curve.

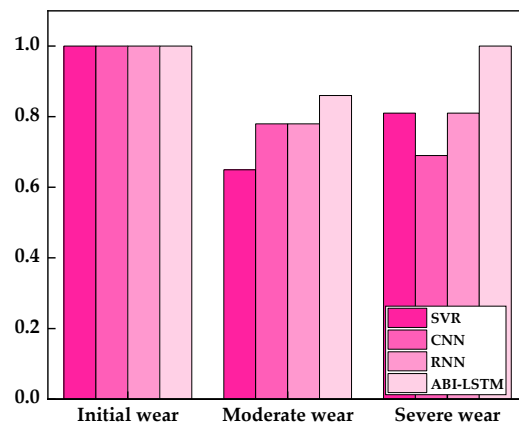


Figure 22. Accuracy of different network structures.

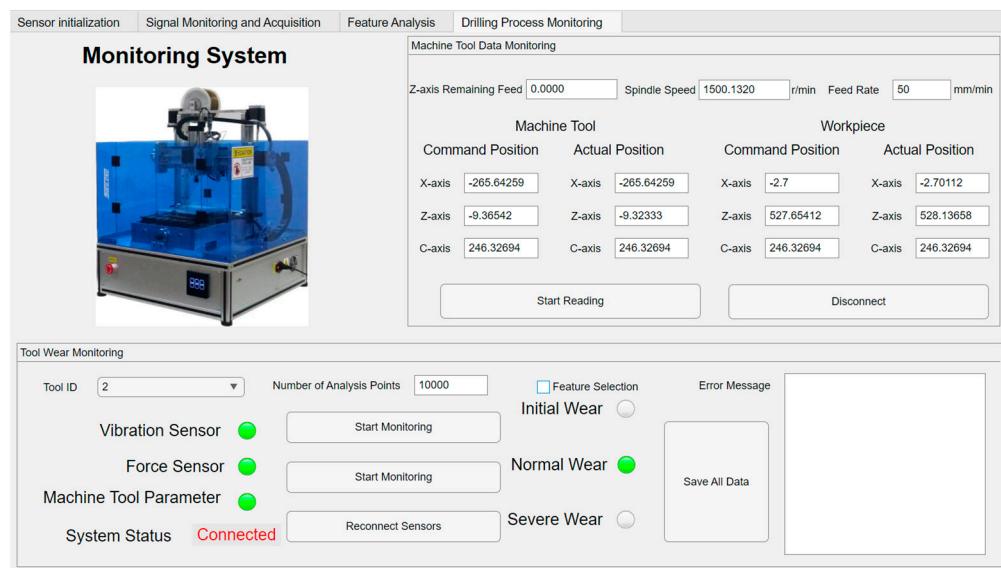


Figure 23. Monitoring interface of the bone material drilling process.

5. Conclusions

This study addresses the issue of tool wear identification during the bone material drilling process by establishing a comprehensive experimental platform that includes data collection, state monitoring, and wear identification. The main achievements include:

Binary cutting mechanism research: through in-depth analysis of the structure, biological characteristics, and mechanical properties of bone materials, this study elucidated the binary cutting mechanism.

Data collection and monitoring platform construction: using force sensors and accelerometers, a data collection and state monitoring experimental platform for the bone material drilling process was constructed. This platform facilitated drilling experiments under actual orthopedic surgical conditions and effectively collected 130 sets of tool wear data.

Feature extraction and analysis: wavelet packet decomposition was utilized to extract time-domain, frequency-domain, and time–frequency domain features. The feature selection process was optimized to reduce correlations among features, resulting in a set of effective feature vectors for subsequent analysis.

Model development and application: an ABI-LSTM model optimized with a multi-head attention mechanism was developed, which, after adjustments, outperformed traditional SVR, CNN, and RNN models in classification performance, achieving efficient tool wear status monitoring.

These achievements not only improve the precision of tool wear identification during the drilling process but also provide technical support for the prevention of thermal damage to bone tissue. Future research will focus on optimizing the real-time performance of the monitoring system and exploring the applicability of various tools and materials to further enhance the system’s universality and practicality.

Author Contributions: Conceptualization, methodology, project administration, L.L.; writing—original draft, data curation, W.K.; resources, supervision, Y.W.; investigation, L.Z. All authors have read and agreed to the published version of the manuscript.

Funding: This study was supported by the National Natural Science Foundation of China (Grant No.51875143).

Institutional Review Board Statement: Harbin University of Science and Technology Biomedical Ethics Approval Document. The manuscript titled “Design of Tool Wear Monitoring System in Bone Material Drilling Process”, authored by Lijia Liu and colleagues and submitted to the journal

“Coatings”, has undergone a review by the Biomedical Ethics Committee. It has been found to conform to ethical principles and has been approved for submission.

Informed Consent Statement: Not applicable.

Data Availability Statement: The data presented in this study are not available due to privacy.

Conflicts of Interest: The authors declare no conflict of interest.

References

- Wang, C.; Chen, Z.; Chen, H.; Song, Q.; Ren, Y.; Sui, J.; Shu, L.; Chen, B.; Zheng, L. A Review on Cutting Mechanism for Bone Material. *Chin. J. Mech. Eng.* **2021**, *57*, 2–32.
- Mauermann, W.J.; Sampathkumar, P.; Thompson, R.L. Sternal Wound Infections. *Best Pract. Res. Clin. Anaesthesiol.* **2008**, *22*, 423–436. [[CrossRef](#)] [[PubMed](#)]
- Allan, W.; Williams, E.D.; Kerawala, C.J. Effects of Repeated Drill Use on Temperature of Bone during Preparation for Osteosynthesis Self-Tapping Screws. *Br. J. Oral Maxillofac. Surg.* **2005**, *43*, 314–319. [[CrossRef](#)] [[PubMed](#)]
- Queiroz, T.P.; Souza, F.Á.; Okamoto, R.; Margonar, R.; Pereira-Filho, V.A.; Garcia, I.R.; Vieira, E.H. Evaluation of Immediate Bone-Cell Viability and of Drill Wear After Implant Osteotomies: Immunohistochemistry and Scanning Electron Microscopy Analysis. *J. Oral Maxillofac. Surg.* **2008**, *66*, 1233–1240. [[CrossRef](#)] [[PubMed](#)]
- Alam, K.; Piya, S.; Al-Ghaithi, A.; Silberschmidt, V. Experimental Investigation on the Effect of Drill Quality on the Performance of Bone Drilling. *Biomed. Eng. Biomed. Tech.* **2020**, *65*, 113–120. [[CrossRef](#)] [[PubMed](#)]
- Hu, Y.; Chen, X.; Chen, J.; Zhang, C.; Fu, W. The Influence of Crescent Texture Parameters on the Axial Force When Drilling Bone. *Med. Eng. Phys.* **2021**, *87*, 87–94. [[CrossRef](#)] [[PubMed](#)]
- Shakouri, E.; Ghorbani Nezhad, M. An in Vitro Study of Bone Drilling: Infrared Thermography and Evaluation of Thermal Changes of Bone and Drill Bit. *Phys. Eng. Sci. Med.* **2020**, *43*, 247–257. [[CrossRef](#)]
- Amewoui, F.; Le Coz, G.; Bonnet, A.-S.; Moufki, A. An Analytical Modeling with Experimental Validation of Bone Temperature Rise in Drilling Process. *Med. Eng. Phys.* **2020**, *84*, 151–160. [[CrossRef](#)] [[PubMed](#)]
- Cao, X.-C.; Chen, B.-Q.; Yao, B.; He, W.-P. Combining Translation-Invariant Wavelet Frames and Convolutional Neural Network for Intelligent Tool Wear State Identification. *Comput. Ind.* **2019**, *106*, 71–84. [[CrossRef](#)]
- Ambadekar, P.K.; Choudhari, C.M. CNN Based Tool Monitoring System to Predict Life of Cutting Tool. *SN Appl. Sci.* **2020**, *2*, 860. [[CrossRef](#)]
- Kumar, M.P.; Dutta, S.; Murmu, N.C. Tool Wear Classification Based on Machined Surface Images Using Convolution Neural Networks. *Sādhanā* **2021**, *46*, 130. [[CrossRef](#)]
- Yao, J.; Lu, B.; Zhang, J. Tool Remaining Useful Life Prediction Using Deep Transfer Reinforcement Learning Based on Long Short-Term Memory Networks. *Int. J. Adv. Manuf. Technol.* **2022**, *118*, 1077–1086. [[CrossRef](#)]
- Liu, X.; Liu, S.; Li, X.; Zhang, B.; Yue, C.; Liang, S.Y. Intelligent Tool Wear Monitoring Based on Parallel Residual and Stacked Bidirectional Long Short-Term Memory Network. *J. Manuf. Syst.* **2021**, *60*, 608–619. [[CrossRef](#)]
- An, Q.; Tao, Z.; Xu, X.; El Mansori, M.; Chen, M. A Data-Driven Model for Milling Tool Remaining Useful Life Prediction with Convolutional and Stacked LSTM Network. *Measurement* **2020**, *154*, 107461. [[CrossRef](#)]
- Wiggins, K.L.; Malkin, S. Orthogonal Machining of Bone. *J. Biomech. Eng.* **1978**, *100*, 122–130. [[CrossRef](#)]
- Wiggins, K.L.; Malkin, S. Drilling of Bone. *J. Biomech.* **1976**, *9*, 553–559. [[CrossRef](#)] [[PubMed](#)]
- Reilly, D.T.; Burstein, A.H. The Elastic and Ultimate Properties of Compact Bone Tissue. *J. Biomech.* **1975**, *8*, 393–405. [[CrossRef](#)] [[PubMed](#)]
- Li, Z.; Yang, Z.; Wang, W.; Guo, Q.; Sun, W.; Han, D.; Liu, X.; Zhang, Y. Ultrasonic Longitudinal Torsion-Assisted Biotic Bone Drilling: An Experimental Study. *Rev. Adv. Mater. Sci.* **2023**, *62*, 20220290. [[CrossRef](#)]
- Pourgiv, S.; Mosavar, A.; Jamshidi, N.; Mohammadi, A. Ultrasonic-Assisted Drilling of Cortical and Cancellous Bone in a Comparative Point of View. *Heliyon* **2024**, *10*, e26248. [[CrossRef](#)]
- Akhbar, M.F.A.; Sulong, A.W. Surgical Drill Bit Design and Thermomechanical Damage in Bone Drilling: A Review. *Ann. Biomed. Eng.* **2021**, *49*, 29–56. [[CrossRef](#)]
- Astakhov, V.P. The Assessment of Cutting Tool Wear. *Int. J. Mach. Tools Manuf.* **2004**, *44*, 637–647. [[CrossRef](#)]
- Astakhov, V.P. *High-Productivity Drilling Tools*; CRC Press: Boca Raton, FL, USA, 2024; ISBN 978-1-00-326331-9.
- Zhang, Z.; Zhang, N.; Wu, F.; Teng, W.; Sun, Y.; Guo, B. Research on Variable Parameter Drilling Method of Ti-CFRP-Ti Laminated Stacks Based on Real-Time Sensing of Drilling Axial Force. *Sensors* **2022**, *22*, 1188. [[CrossRef](#)] [[PubMed](#)]
- International Standard ISO 3685*; Tool-Life Testing with Single-Point Turning Tools. ISO: Geneva, Switzerland, 1993.
- Islam, M.A.; Kamarrudin, N.S.; Daud, R.; Mohd Noor, S.N.F.; Azmi, A.I.; Razlan, Z.M. A Review of Surgical Bone Drilling and Drill Bit Heat Generation for Implantation. *Metals* **2022**, *12*, 1900. [[CrossRef](#)]
- Prasannavenkadesan, V.; Pandithivan, P. Mechanistic Models to Predict Thrust Force and Torque in Bone Drilling: An In-Vitro Study Validated with Robot-Assisted Surgical Drilling Parameters. *Proc. Inst. Mech. Eng. Part E J. Process Mech. Eng.* **2021**, *235*, 1984–1997. [[CrossRef](#)]

27. Wang, W.; Shi, Y.; Yang, N.; Yuan, X. Experimental Analysis of Drilling Process in Cortical Bone. *Med. Eng. Phys.* **2014**, *36*, 261–266. [[CrossRef](#)] [[PubMed](#)]
28. Sridhar, A.V.; Prasad, B.S.; Mouli, K.V.V.N.R.C. Evaluation of Tool Performance and Wear through Vibration Signature Analysis in Drilling of IS3048 Steel. *J. Eng. Appl. Sci.* **2021**, *68*, 27. [[CrossRef](#)]
29. Huang, Z.; Zhu, J.; Lei, J.; Li, X.; Tian, F. Tool Wear Predicting Based on Multi-Domain Feature Fusion by Deep Convolutional Neural Network in Milling Operations. *J. Intell. Manuf.* **2020**, *31*, 953–966. [[CrossRef](#)]
30. Zolfaghari, S.; Noor, S.B.M.; Rezazadeh Mehrjou, M.; Marhaban, M.H.; Mariun, N. Broken Rotor Bar Fault Detection and Classification Using Wavelet Packet Signature Analysis Based on Fourier Transform and Multi-Layer Perceptron Neural Network. *Appl. Sci.* **2018**, *8*, 25. [[CrossRef](#)]

Disclaimer/Publisher’s Note: The statements, opinions and data contained in all publications are solely those of the individual author(s) and contributor(s) and not of MDPI and/or the editor(s). MDPI and/or the editor(s) disclaim responsibility for any injury to people or property resulting from any ideas, methods, instructions or products referred to in the content.